APPLIED SCIENCES AND ENGINEERING

Superior fracture resistance and topology-induced intrinsic toughening mechanism in 3D shell-based lattice metamaterials

Yujia Wang[1,2], Kunlin Wu[2], Xuan Zhang[3], Xiaoyan Li[4]*, Yifan Wang[2]*, Huajian Gao[1,2,4]*

Lattice metamaterials have demonstrated remarkable mechanical properties at low densities. As these architected materials advance toward real-world applications, their tolerance for damage and defects becomes a limiting factor. However, a thorough understanding of the fracture resistance and fracture mechanisms in lattice metamaterials, particularly for the emerging shell-based lattices, has remained elusive. Here, using a combination of in situ fracture experiments and finite element simulations, we show that shell-based lattice metamaterials with Schwarz P minimal surface topology exhibit superior fracture resistance compared to conventional octet truss lattices, with average improvements in initiation toughness up to 150%. This superiority is attributed to the unique shell-based architecture that enables more efficient load transfer and higher energy dissipation through material damage, structural plasticity, and material plasticity. Our study reveals a topology-induced intrinsic toughening mechanism in shell-based lattices and highlights these architectures as a superior design route for creating lightweight and high-performance mechanical metamaterials.

INTRODUCTION

Lightweight yet mechanically robust materials are in high demand for a wide range of applications, such as components in aircraft, vehicle, energy storage devices, heat exchangers, and medical implants (*1*–*3*). Despite the substantial demand, it remains challenging to create materials that simultaneously have low density and high mechanical performance, as these properties are often mutually exclusive (*1*). Lattice metamaterials with ordered and rationally designed architectures have demonstrated amazing properties in overcoming these trade-offs (*4*, *5*), exemplifying a paradigm shift called mechanomaterials where designed geometries are proactively deployed to program material properties (*6*, *7*). Over the past decades, extensive efforts have been devoted to demonstrating remarkable elastic and plastic properties of lattice metamaterials at low densities, such as high modulus (*8*–*12*), exceptional strength (*13*–*16*), excellent recoverability (*16*–*18*), high energy absorption (*18*, *19*), and remarkable dynamic impact resilience (*20*–*22*). In contrast, their fracture behaviors have remained largely underexplored. For practical applications of structural materials, fracture toughness is often considered as a limiting factor as it represents the material's ability to resist fracture in the presence of cracks and defects, which are often inevitably introduced during manufacturing or service (*23*). Most existing studies on the fracture of lattice metamaterials have so far been restricted to two-dimensional (2D) lattices (*24*–*27*). Only with recent advances in additive manufacturing techniques have there been increasing studies on characterizing the fracture resistance of 3D truss-based lattices, with the octet truss lattice as a prime example (*28*–*34*). Although truss-based architectures have dominated lattice metamaterials for the past two decades, a recent report suggests that shell-based architectures may provide a superior design route to achieving uniform strain energy distribution and ultrahigh specific strength (*35*). Other recent studies have also revealed a capability of shell-based lattices to attain a range of desirable mechanical properties, such as high energy absorption (*36*), extraordinary mechanical resilience (*37*), and tunable anisotropy (*38*, *39*). Nevertheless, a thorough understanding of the fracture behaviors of 3D shell-based lattices still remains elusive.

Here, we investigate the fracture behaviors of shell-based lattices with the Schwarz P minimal surface topology (*40*, *41*) and provide a comprehensive comparison of their fracture behaviors with those of traditional octet truss (*42*) lattices. We fabricate compact tension (CT) specimens of both octet truss and Schwarz P shell lattices using projection microstereolithography (PμSL) and subject the fabricated specimens to in situ fracture tests. Experimental results indicate that Schwarz P shell lattices exhibit superior fracture initiation toughness that outperforms octet truss lattices by up to 150% at the same relative densities, as well as demonstrate enhanced resistance to crack propagation. The superior fracture resistance can be attributed to larger plastic zone and fracture process zone sizes in Schwarz P shell lattices, as evidenced by a digital image correlation (DIC) analysis. We further perform finite element (FE) simulations, with results indicating that the Schwarz P shell lattices can distribute stress more uniformly and thereby enable a greater number of material elements to access the high-stress region and participate in the fracture process, resulting in higher energy dissipation. Our study demonstrates that shell-based lattices can be more promising candidates for achieving exceptional fracture toughness in the low-density regime.

RESULTS

Design, fabrication, and mechanical testing

We fabricated CT specimens using PμSL to investigate and compare the fracture resistance of octet truss and Schwarz P shell lattices, which serve as representative examples from truss-based and shell-based

[1]Institute of High Performance Computing (IHPC), Agency for Science, Technology and Research (A*STAR), Singapore 138632, Singapore. [2]School of Mechanical and Aerospace Engineering, College of Engineering, Nanyang Technological University, 70 Nanyang Drive, Singapore 639798, Singapore. [3]Department of Advanced Manufacturing and Robotics, College of Engineering, Peking University, Beijing 100871, China. [4]Mechano-X Institute, Applied Mechanics Laboratory, Department of Engineering Mechanics, Tsinghua University, Beijing 100084, China.
*Corresponding author. Email: xiaoyanlithu@tsinghua.edu.cn (X.L.); yifan.wang@ntu.edu.sg (Yifan Wang); gao.huajian@tsinghua.edu.cn (H.G.)

architecture categories, respectively. The Schwarz P topology is a prominent example of triply periodic minimal surfaces (TPMSs), which are smooth and nonintersecting surfaces with zero mean curvature everywhere (*40*, *41*). Figure 1 (A and B) shows the computer-aided design models of octet truss and Schwarz P shell unit cells. The Schwarz P shell unit cell was constructed via the Surface Evolver software (*43*) with subsequent smoothing and thickening (*35*). The CT specimens were designed with dimensions in accordance with the American Society for Testing and Materials (ASTM) standard E1820 (*44*), and precracks were directly introduced during fabrication as shown in Fig. 1 (C and D) (see Materials and Methods for details). We tailored the relative densities of the fabricated lattices by varying the beam diameters or shell thicknesses while maintaining a constant unit cell length of 1.5 mm. This allows the obtained octet truss and Schwarz P shell lattices to retain comparable relative densities within the ranges of 9.0 to 42.7% and 11.5 to 39.2%, respectively.

We conducted in situ fracture tests on the fabricated specimens (see Materials and Methods for details). Figure 1E shows representative force-displacement curves of octet truss and Schwarz P shell lattices with different relative densities. All of the curves exhibit three characteristic regions: elastic, plastic, and failure. During loading, the force first increased linearly with increasing displacement and then exhibited a nonlinear dependence that can be attributed to plastic deformation around the crack tip. Once reaching the peak force, fracture initiation occurred and the crack gradually propagated due to the inherent discreteness of the lattice materials, resulting in the multiple force drops in the force-displacement curves. Comparing octet truss and Schwarz P shell lattices with comparable relative densities, it can be seen that the latter exhibited a higher peak force as well as a larger corresponding displacement at the peak force (Fig. 1E), implying a superior fracture resistance of the Schwarz P shell design.

Fracture properties and behaviors

To quantitatively analyze their fracture properties, we extracted the peak force and corresponding displacement at the peak force from the force-displacement curves of all of the tested samples. As shown in Fig. 2 (A and B), both octet truss and Schwarz P shell lattices exhibit an increase in the peak force with increasing relative density, while the displacement at the peak force decreases as the relative density increases. Over the entire range of relative densities that we investigated, the Schwarz P shell lattices consistently exhibit a higher peak force than the octet truss lattices, indicating that a higher force is required to initiate fracture in the former. Notably, the displacement at the peak force of the Schwarz P shell lattices is also larger than that of the octet truss lattices, suggesting delayed fracture initiation in the former. We also estimated the energy required for complete fracture. Since the force remained a nonzero value after the test, we integrated the force-displacement curve until the point at which the force decreased to 10% of the peak force, as illustrated in Fig. 2C. The results indicate that the Schwarz P shell lattices exhibit an average enhancement in energy to fracture from 210 to 286% compared to the octet truss lattices in the same relative density range.

We further calculated the fracture initiation toughness using the *J*-integral method in accordance with ASTM E1820 (*44*) (see Materials and Methods for details). Figure 2D shows that Schwarz P shell lattices achieved significantly higher fracture initiation toughness, surpassing octet truss lattices by 83 to 150%. To determine the fracture toughness of the constituent material, we also fabricated and tested fully dense solid CT specimens with the same overall dimensions as the lattice CT specimens (fig. S1). The material toughness was calculated using the same method and is also plotted in Fig. 2D. It can be seen that both octet truss and Schwarz P shell lattices exhibit higher toughness than the values predicted by a linear relationship between toughness and relative density. Moreover, Schwarz P shell lattices with $\bar{\rho} \approx 38.0\%$ achieved higher toughness than the constituent material while maintaining a 62.0% reduction in weight. The results suggest that the shell-based lattice metamaterials have substantial potential for being designed to achieve exceptional fracture resistance in the low-density regime.

We also obtained crack growth resistance curves, the so-called *J-R* curves, as shown in Fig. 3A (see Materials and Methods for more details). The *J-R* curves plot the *J*-integral as a function of crack

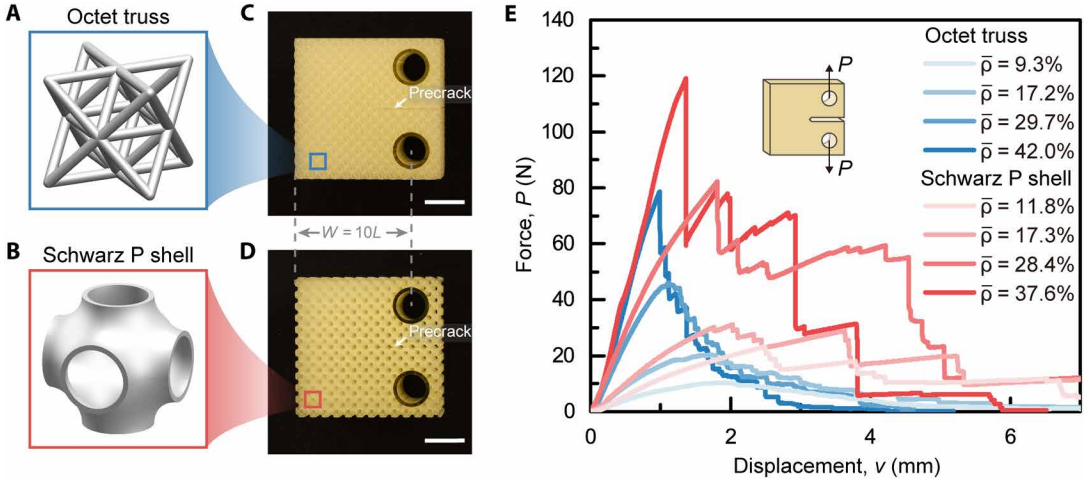

Fig. 1. Fracture experiments on lattice metamaterials with octet truss and Schwarz P shell topologies. (**A** and **B**) Computer-aided design models of octet truss and Schwarz P shell unit cells. (**C** and **D**) Optical images of CT specimens of octet truss and Schwarz P shell lattices fabricated by PμSL, with design in accordance with the ASTM standard. Scale bars, 5 mm. (**E**) Representative force-displacement curves of octet truss and Schwarz P shell lattices with different relative densities.

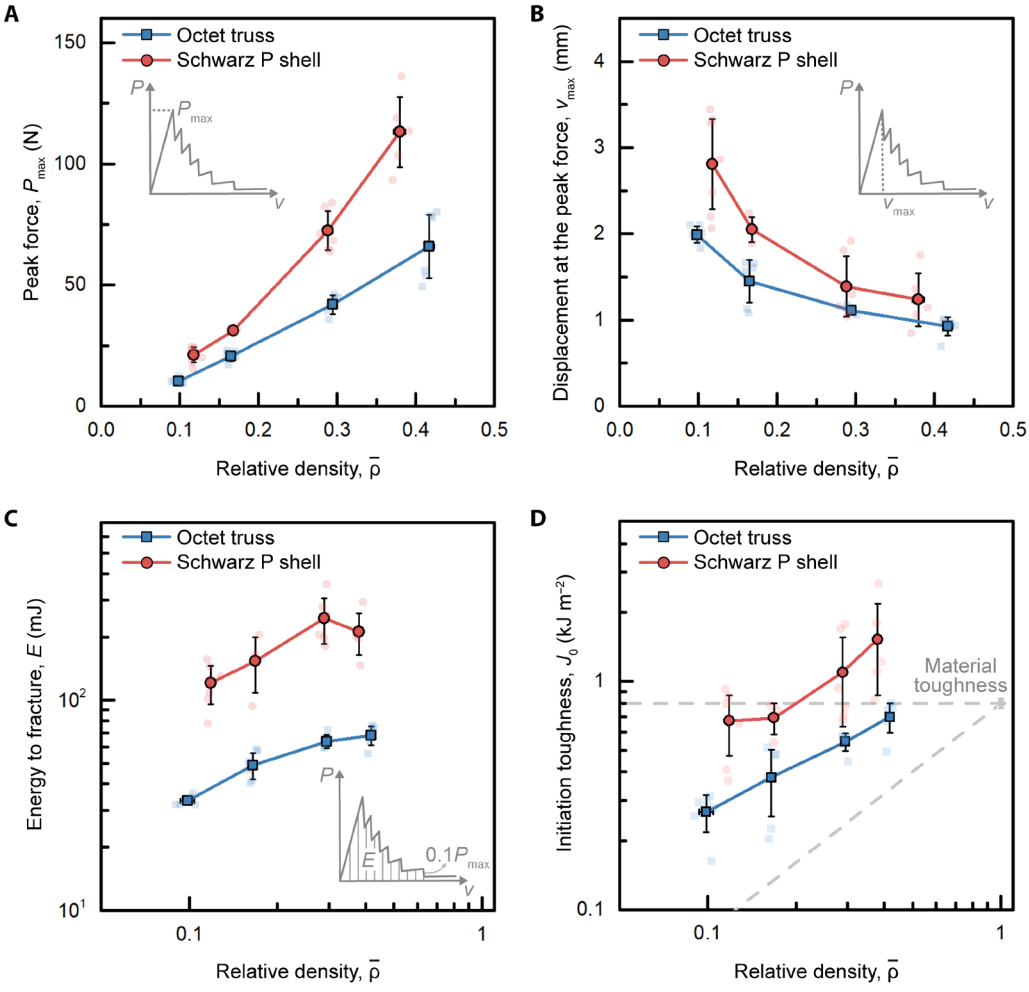

Fig. 2. Fracture properties of octet truss and Schwarz P shell lattices. (**A** and **B**) Peak force and corresponding displacement versus relative density maps, respectively. The peak force and corresponding displacement are extracted from the force-displacement curves, as illustrated in the insets. (**C**) Log-log plots of energy to fracture versus relative density for octet truss and Schwarz P shell lattices. The energy to fracture is defined as the area under the force-displacement curve until the force decreases to $0.1P_{max}$, as illustrated in the inset. (**D**) Log-log plots of initiation toughness versus relative density for octet truss and Schwarz P shell lattices. The initiation toughness is calculated as the *J*-integral at the crack initiation, following the ASTM E1820 standard. The gray diamond marker denotes the toughness of the solid constituent material. The horizontal and slanted gray dashed lines are defined by the material toughness and slopes of zero and one, respectively. In (A) to (D), the error bar of each data point is the standard deviation from the statistical average for three to seven experimental samples, with values depicted by the lighter-colored scatter points.

extension and serve as a measure of a material's ability to resist catastrophic failure. During the in situ fracture testing, both octet truss and Schwarz P shell lattices exhibited more stable crack growth compared to the catastrophic fracture observed in the fully dense solid constituent material (movies S1 to S3). In the lattice materials, cracks were periodically arrested by the void spaces in a unit cell, resulting in multiple force drops in the force-displacement curves (Fig. 1E). As shown in Fig. 3A, the octet truss lattices exhibit relatively flat and even falling *J*-*R* curves after the first crack extension. Figure 3 (B to E) shows representative snapshots of octet truss lattices with different relative densities during crack propagation. Additional snapshots of the fracture process in octet truss lattices, shown in fig. S2, consistently exhibit planar mode I crack paths. In comparison, Schwarz P shell lattices with relative densities of ~11.8 and ~17.3% exhibit rising *R*-curves, indicative of a higher driving force required for further crack propagation and, hence, a higher resistance to crack extension. For Schwarz P shell lattices with higher relative densities (~28.4 and ~37.6%), we observed relatively fewer and larger crack extensions. Although their fracture resistance decreases after two crack extensions, it remains significantly higher than that of the octet truss lattices at comparable relative densities (Fig. 3A). Typical images in Fig. 3 (F to I) and detailed snapshots in fig. S3 show that Schwarz P shell lattices exhibit more complicated fracture characteristics and tortuous crack paths, with frequently observed crack deflection and crack branching. As a result, the Schwarz P shell lattices demonstrated higher force and larger load-line displacement at the same crack extension compared to the octet truss lattices at comparable relative densities (movies S2 and S3), implying superior fracture resistance of the former.

We further performed fractography using scanning electron microscopy (SEM). The SEM images of fracture surfaces in the octet truss lattice suggest that most of the beams fail near the nodes in the lattice (Fig. 3J), and the fracture surface of individual beam is relatively smooth as shown in Fig. 3 (K and L). In contrast, the

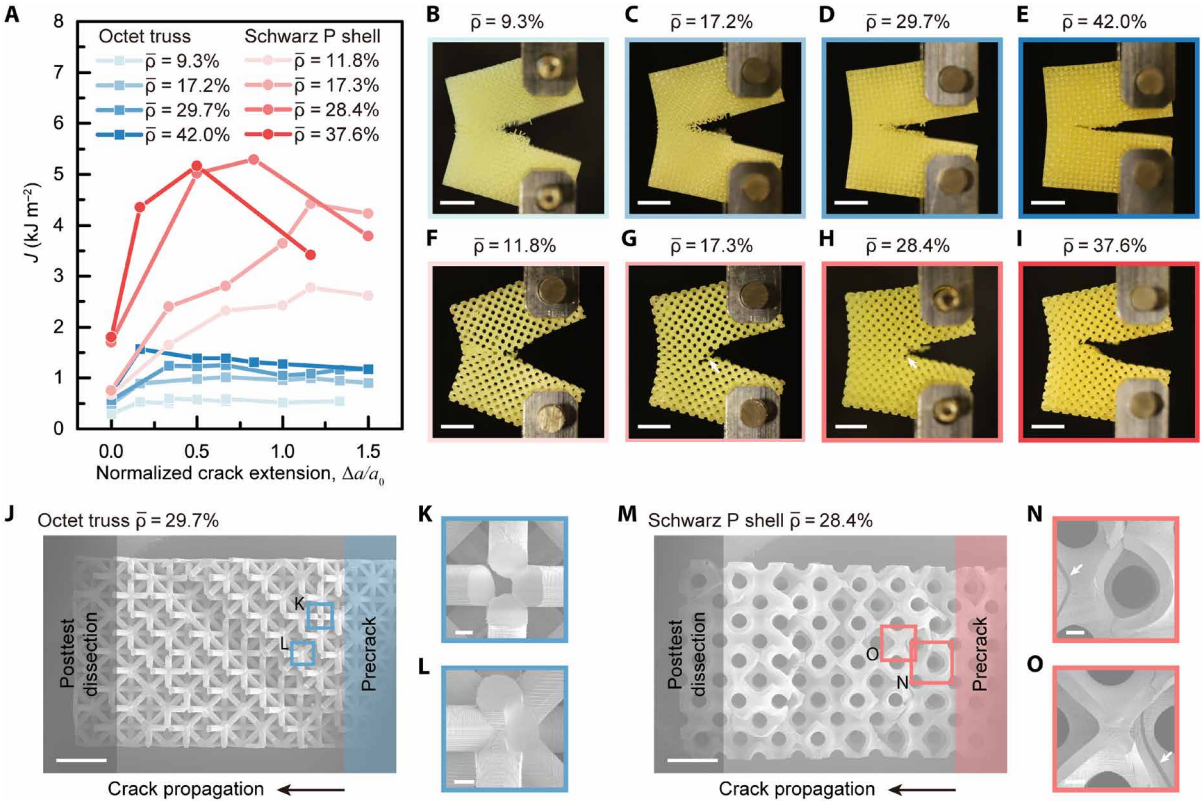

Fig. 3. Fracture resistance and crack propagation. (**A**) Representative *J-R* curves for octet truss and Schwarz P shell lattices with different relative densities. (**B** to **E**) Snapshots of octet truss lattices during crack propagation. Scale bars, 5 mm. (**F** to **I**) Snapshots of Schwarz P shell lattices during crack propagation. Scale bars, 5 mm. (**J** to **L**) Scanning electron microscopy (SEM) fractography of an octet truss lattice with a relative density of 29.7%. These images show that most beams fail near the nodes in the octet truss lattice. Scale bars, 2 mm (J) and 100 μm (K and L). (**M** to **O**) SEM fractography of the Schwarz P shell lattice with a relative density of 28.4%. These images indicate more tortuous crack paths and rougher fracture surfaces in the Schwarz P shell lattice. Scale bars, 2 mm (M) and 200 μm (N and O). The arrows in (G), (H), (N), and (O) indicate crack deflection in Schwarz P shell lattices.

Schwarz P shell lattices exhibit more intricate and rougher fracture surfaces compared to the octet truss lattices (Fig. 3, M to O). We estimated the total areas of fracture surfaces in Fig. 3 (J and M), with results indicating a larger fracture surface area in the Schwarz P shell lattice compared to the octet truss lattice at a comparable relative density (fig. S4). Therefore, it can be inferred that higher energy dissipation creates rougher and larger fracture surfaces in the Schwarz P shell lattices, leading to superior fracture resistance.

FE simulations, DIC analysis, and fracture mechanisms

To further understand the underlying mechanisms for the superior fracture resistance of shell-based lattices, we first performed FE simulations that mimic experimental tests on the CT specimens. To mitigate computational costs for simulating crack propagation in these lattice materials, we used beam and shell elements to model octet truss and Schwarz P shell lattice geometries, respectively (see Materials and Methods for more details), and focused on lattices with low relative densities (5.2 to 21.2%). The corresponding force-displacement curves and *J-R* curves are presented in fig. S5. The normalized fracture toughness from FE simulations is in good agreement with that obtained from experiments (fig. S5C). Figure 4 (A and B) shows von Mises stress distributions in octet truss and Schwarz P shell lattices with a similar relative density of ~21%, just before the onset of fracture. It is seen that the Schwarz P shell lattice exhibits a higher proportion of constituent material elements undergoing plastic deformation. The volume fractions of elements surpassing the yield strength of the constituent material are 1.7 and 6.7% for octet truss and Schwarz P shell lattices with the relative density of ~21%, respectively, and similar trend holds at other densities (fig. S5D). This difference can be attributed to the unique architecture of shell-based lattices, which promotes more uniform stress distribution. As a result, a larger number of material elements undergo plastic deformation in Schwarz P shell lattices compared to that in octet truss lattices, where significant stress concentration occurs at nodes. Figure 4 (C and D) shows the equivalent plastic strain distributions in the two lattices during later stages of crack propagation. Here, the equivalent plastic strain has been normalized by the plastic strain of the constituent material at fracture (i.e., equivalent plastic strain at damage initiation of the constituent material). In the octet truss lattice, only elements near the nodes reach the material fracture strain and, consequently, undergo damage, consistent with the nodal failures observed in experiments. In contrast, a larger volume of material attains the fracture strain in the Schwarz P shell lattice. These results suggest that the shell-based architecture can enable a greater number of material elements to participate in the fracture process, thereby contributing to its superior fracture resistance during crack propagation.

To characterize the plastic zone and fracture process zone in our experiments, we performed DIC analysis using the open-source

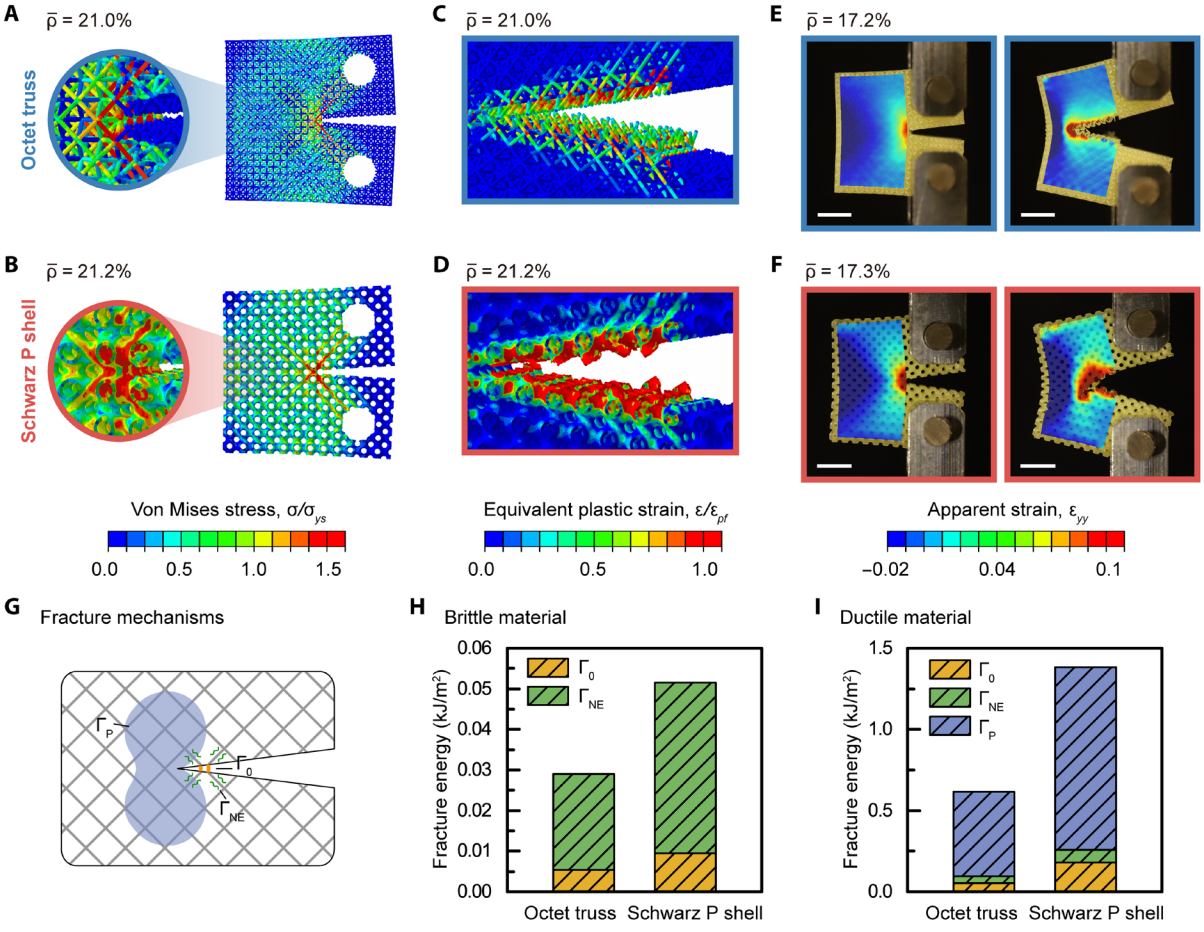

Fig. 4. FE simulations and DIC analysis. (**A** and **B**) Von Mises stress distributions just before the onset of fracture in octet truss and Schwarz P shell lattices with a similar relative density of ~21% from FE simulations (with beam and shell elements). The von Mises stress is normalized by the yield stress of the constituent material. (**C** and **D**) Equivalent plastic strain distributions in octet truss and Schwarz P shell lattices with a similar relative density of ~21% from FE simulations (with beam and shell elements). The equivalent plastic strain is normalized by the plastic strain of the constituent material at damage initiation. (**E** and **F**) DIC maps at the moment of fracture initiation and at a later stage of crack propagation in octet truss and Schwarz P shell lattices with relative density of 17.2 and 17.3%, respectively. Scale bars, 5 mm. FE simulations and DIC analysis demonstrate larger plastic zone and fracture process zone sizes in the Schwarz P shell lattice. (**G**) Schematic of fracture mechanisms in lattice materials. (**H** and **I**) Fracture energy decoupling from FE simulations using brittle and ductile material behaviors, respectively (with solid elements).

DIC package Ncorr (*45*). Figure 4 (E and F) presents DIC maps of the apparent vertical strain component for octet truss and Schwarz P shell lattices. The left maps in Fig. 4 (E and F) correspond to the moment of fracture initiation. Although somewhat qualitative, these maps demonstrate a significantly larger plastic zone size in the Schwarz P shell lattice. Moreover, the Schwarz P shell lattice also exhibits a larger fracture process zone size during crack propagation (right maps in Fig. 4, E and F). Note that the DIC analysis is conducted at a level that treats the lattice structures as metamaterials, while FE simulations provide more detailed insights at the material level. The combined results from our FE simulations and DIC analysis qualitatively reveal larger plastic zone and fracture process zone sizes in the Schwarz P shell lattices.

We further provide a quantitative understanding of the fracture mechanisms in lattice materials (Fig. 4G). Essentially, the fracture energy Γ of a lattice metamaterial can be expressed as

$$\Gamma = \Gamma_0 + \Gamma_{NE} + \Gamma_P \quad (1)$$

In Eq. 1, Γ_0 denotes the intrinsic fracture energy associated with material failure on the crack path. For a lattice constructed from an ideally brittle material, Γ_0 is the energy required to create new surfaces per unit crack area and thus theoretically proportional to the material's surface energy γ, expressed as $\Gamma_0 = k \cdot 2\gamma$, where the proportional coefficient k depends on the lattice topology. As shown in fig. S6, the Schwarz P shell lattice has a larger proportional coefficient k than the octet truss lattice at the same relative density due to its larger fracture surface area within one unit cell, which suggests a higher intrinsic fracture energy of the former. Γ_{NE} represents the nonrecoverable elastic energy that is transformed into vibration of the lattice structure and eventually dissipated. In lattice materials, fracture of discrete elements near the crack tip can lead to dynamic perturbations in the state of their neighbors. The stored elastic energy is then partially converted into kinetic energy and ultimately dissipated as heat or acoustic energy. In this regard, Γ_{NE} represents a unique fracture dissipation mechanism in lattice materials that is distinct from bulk materials, which can be referred to as "structural plasticity." Γ_P represents the energy dissipation due to material

plasticity and does not exist when the lattice is constructed from an ideally brittle material.

We then numerically decoupled the contributions from these mechanisms. Note that our FE simulations using beam and shell elements cannot accurately represent the real fracture surfaces and hence do not allow for the accurate calculation of intrinsic fracture energy associated with material failure. To quantitatively identify contributions from material failure as well as other mechanisms, we performed additional FE simulations using solid elements for both octet truss and Schwarz P shell lattices (see Materials and Methods for more details). We considered two types of constitutive material behaviors: one corresponding to a brittle material and the other exhibiting a ductile material behavior, the same as that used in FE simulations of beam and shell elements (see Materials and Methods for more details). For lattice structures constructed from an ideally brittle material, the fracture energy can be expressed as the summation of the first two terms on the right of Eq. 1, i.e., $\Gamma = \Gamma_0 + \Gamma_{NE}$. Figure 4H shows the comparison in fracture energies between octet truss and Schwarz P shell lattices at the same relative density of ~30%. The Schwarz P shell lattice has a higher Γ_0 than the octet truss lattice, which can be attributed to a larger volume of material elements in the fracture process zone in the former (fig. S7). In addition to Γ_0, the nonrecoverable elastic energy Γ_{NE} is also magnified by the Schwarz P shell topology, resulting in its higher total fracture energy compared to the octet truss lattice. Notably, Γ_{NE} comprises a larger proportion in the total fracture energy compared to Γ_0 for both lattices, indicating the significant role of Γ_{NE} in the fracture energy of lattice materials when the constitutive material behavior is brittle. Figure 4I indicates that all of the three terms—Γ_0, Γ_{NE}, and Γ_P—of the Schwarz P shell lattice are higher than those of the octet lattice with ductile material behavior similar to that of the material used in our experiments. The von Mises stress distributions just before the onset of fracture (fig. S8) indicate that the Schwarz P shell lattice enables more uniform stress distribution and allows more material elements to attain higher stress, resulting in greater volumes of material in plastic and fracture process zones (table S1). Our results provide a comprehensive understanding of the underlying mechanisms for the superior fracture resistance of shell-based lattices: Their unique topology results in higher energy dissipation through a combination of material damage, structural plasticity, and material plasticity.

DISCUSSION

Recent studies have suggested that the mechanical properties of architected materials mainly depend on their topology, feature sizes, and constituent materials (*5*). In the current study, we focused on the dependence of the fracture behaviors of lattice metamaterials on topology. We have demonstrated that Schwarz P shell lattices exhibit superior fracture resistance than octet truss lattices when constructed from the same material and having identical sample dimensions and relative densities. Here, we also compared the fracture toughness K_{IC} of our fabricated lattices with that of existing materials (details for the K_{IC} calculation are provided in Materials and Methods). As shown in an Ashby map of fracture toughness versus density (Fig. 5A), in the lightweight regime (density < 1000 kg m^{-3}), our polymer octet truss and Schwarz P shell lattices outperform existing polymer and ceramic foams while competing favorably with metal foams and certain natural materials. This suggests the potential for constructing shell-based lattices using metals to achieve higher toughness while maintaining low densities. Figure 5B provides a comparison of the normalized fracture toughness of our polymer octet truss and Schwarz P shell lattices with other existing 3D lattice metamaterials (*28*–*34*). The normalized fracture toughness

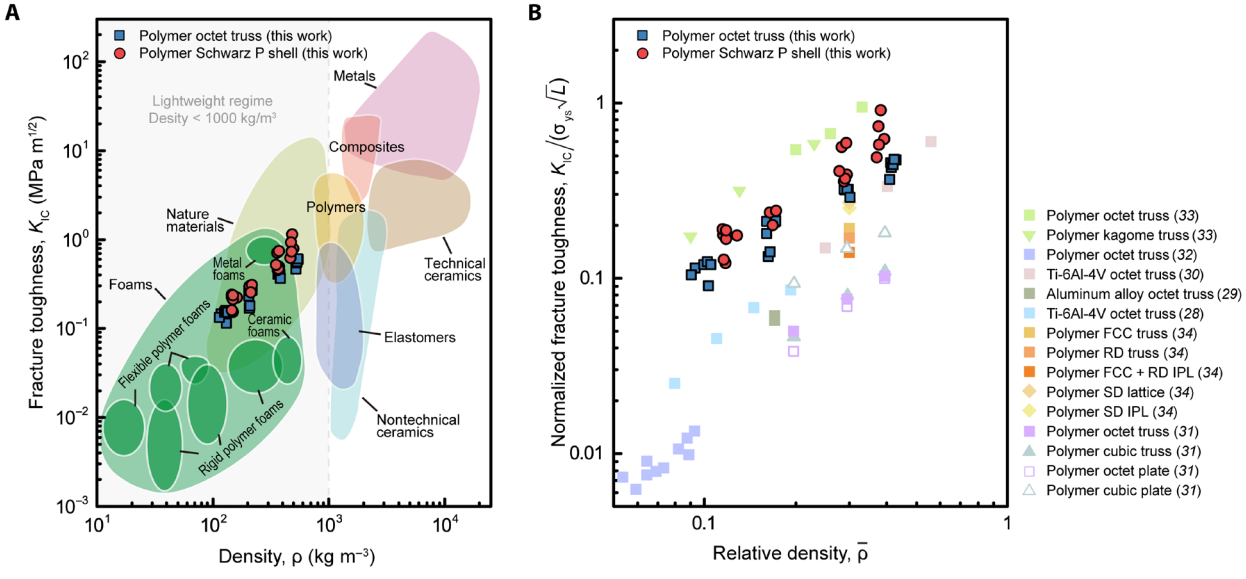

Fig. 5. Comparison of the fracture toughness of our lattice metamaterials with existing materials. (**A**) The Ashby map of fracture toughness versus density. (**B**) Normalized fracture toughness versus relative density for our polymer octet truss and Schwarz P shell lattices and other 3D lattice metamaterials that have been reported to date, including Ti-6Al-4V octet truss lattices (*28*, *30*), aluminum alloy octet truss lattices (*29*), polymer truss- and plate-based lattices (*31*), polymer octet truss lattices fabricated via PμSL (*32*), polymer octet and kagome truss microlattices fabricated via two-photon lithography (TPL) (*33*), and polymer face-centered cubic (FCC), rhombic dodecahedron (RD), Schwarz D (SD) truss-based lattices and interpenetrating lattices (IPL) (*34*).

is expressed as $\overline{K}_{IC} = K_{IC} / \left(\sigma_{ys}\sqrt{L}\right)$, where σ_{ys} is the yield strength of the constituent material and L is the unit cell length. Our polymer octet truss and Schwarz P shell lattices exhibit higher normalized fracture toughness than most existing polymer and metal truss- and plate-based lattices, except for the polymer octet and kagome truss microlattices fabricated from IP-Dip using two-photon lithography (TPL), with feature sizes down to 1.03 to 2.25 μm (*33*). This difference can be attributed to the variations in constituent materials and characteristic size scales, as discussed further below.

Previous theoretical studies (*1*, *25*) on 2D truss-based lattices suggest that the normalized fracture toughness scales with the relative density as $\overline{K}_{IC} = D\overline{\rho}^{d}$, where D and d are constants. We applied this relationship to fit our experimental and numerical results and obtained the coefficient D and the exponent d for our octet truss and Schwarz P shell lattices. The obtained coefficients and scaling exponents, along with those from existing studies, are summarized in table S2. The scaling exponents obtained from our FE simulations are in good agreement with those from experimental data. Both octet truss and Schwarz P shell lattices exhibit scaling exponents close to one, while Schwarz P shell lattices have a higher value of the coefficient D than octet truss lattices, which is associated with the higher fracture toughness of Schwarz P shell lattices. Previous theoretical studies (*1*, *25*) based on linear elastic fracture mechanics have suggested that, for elastic-brittle lattices, the constants D and d are dependent on the lattice topology. In table S2, it is evident that lattices with the same octet truss topology exhibit similar values of scaling exponents around one but varying coefficients, which is also reflected by the variation in the normalized fracture toughness of the octet truss lattices, as shown in Fig. 5B. This variation can be attributed to the different behaviors of their constituent materials. According to the theoretical analysis (*27*) based on elastic-plastic fracture mechanics, for elastoplastic 2D lattices composed of materials exhibiting behaviors described by the Ramberg-Osgood relationship, the relationship between the fracture toughness and relative density can be expressed as

$$K_{IC} / \left(\sigma_{ys}\sqrt{L}\right) = D'\overline{\rho}^{d}\left(\varepsilon_f/\varepsilon_{0s}\right)^{\frac{n+1}{2n}} \quad (2)$$

where ε_f and ε_{0s} are the fracture strain and yield strain of the constituent material, respectively, and n is the strain hardening exponent. The results indicate that the scaling exponent d remains the same as in elastic-brittle cases. However, the coefficient between the normalized fracture toughness and $\overline{\rho}^{d}$ is significantly influenced by the material behavior, with a direct dependence on the term $\left(\varepsilon_f/\varepsilon_{0s}\right)^{\frac{n+1}{2n}}$. Furthermore, D' can also be sensitive to the value of n for the same lattice topology (*27*). Therefore, the higher normalized fracture toughness of octet truss lattices fabricated via TPL can be attributed to the larger fracture strain (>0.3) of the IP-Dip polymer used in TPL (*33*). The strong dependence of the coefficient on the material behaviors suggests the potential for tuning the fracture toughness of lattice metamaterials by selecting suitable constituent materials.

In addition to the constituent materials, characteristic size scale can also play an important role in the fracture toughness of lattice metamaterials. The aforementioned scaling law implies that a reduction in the length scale, corresponding to smaller unit cell lengths, may lead to decreased fracture toughness. However, it should be noted that, in practice, a smaller length scale often results in fewer flaws and defects in the material. For example, previous research has shown that smaller-scale microlattices fabricated via TPL exhibit higher normalized strength than their larger-scale counterparts fabricated via PμSL (*35*). The size effects on the mechanical properties of the constituent materials can also contribute to the fracture resistance of lattice metamaterials. Therefore, the smaller size scale could be another reason responsible for the higher normalized fracture toughness of truss-based lattices fabricated via TPL (Fig. 5B) (*33*). In our current study, we observed that Schwarz P shell lattices with lower relative densities exhibited rising *R*-curves, which differs from their high relative density counterparts. This might be attributed to the strong size effect of the constituent material (*46*). On the other hand, the scaling law also suggests that the fracture toughness can be improved by increasing the unit cell length L, which suggests an opportunity to leverage structural hierarchy to enhance the fracture toughness of lattice metamaterials. The influence of characteristic size scales on the fracture behaviors of lattice metamaterials, including size effects at micro/nanoscales and structural hierarchy, remains largely unexplored and deserves further investigation.

Here, we have focused on comparing truss-based and shell-based lattices, selecting octet truss and Schwarz P shell topologies as they are the most widely investigated and prominent examples within their respective categories. While there are many existing studies on the fracture properties of octet truss lattices, the investigation on fracture properties of shell-based lattices is still in its early stages. Given the large number of TPMS topologies, exploring and comparing the fracture behaviors of various shell-based designs is a promising direction for future research. We also performed additional in situ fracture experiments and FE simulations on another type of shell-based lattice with I-WP (Schoen's I-graph–wrapped package) minimal surface topology to illustrate this potential direction. As shown in fig. S9, I-WP shell lattices exhibit initiation toughness slightly lower than Schwarz P shell lattices yet still significantly higher than that of octet truss lattices. Similar to Schwarz P shell lattices, I-WP shell lattices demonstrate larger plastic zone and fracture process zone sizes compared to octet truss lattices (see fig. S10 and Fig. 4). The differences in fracture behaviors between Schwarz P and I-WP shell lattices include higher slopes of force-displacement curves and smaller displacements at peak force for the latter (figs. S9E and S10C). FE simulations indicate that I-WP shell lattices exhibit comparable normalized fracture toughness $\overline{K}_{IC}$ to Schwarz P shell lattices (fig. S10D). Because of the higher modulus of I-WP shell lattices, their initiation toughness J_0 is lower than that of Schwarz P shell lattices, consistent with experimental results (fig. S9F). Future research can further explore and compare the fracture behaviors of various shell-based topologies to identify the optimal architecture designs for enhanced fracture resistance.

In the current study, we have revealed the topology-induced intrinsic toughening mechanism in lattice metamaterials and thereby offer a design principle for tough architected materials, which involves engineering their topology to magnify fracture surface area, structural dissipation, and material plastic dissipation. While our experiments were conducted with a polymer exhibiting some plasticity, our simulations suggest that this design principle is applicable to brittle materials as well, offering potential for toughening structural materials like carbon and ceramics. Moreover, the smooth and continuous topology of shell-based architectures provides a sufficiently rich design space to realize additional extrinsic toughening mechanisms. This potential exploration may lead to even more

superior fracture resistance, which is a direction deserving future investigation. Compared to the established composite strategies that combine hard and soft materials into intricate solid structures, the topology-induced toughening strategy in lattice metamaterials offers the advantages of achieving ultralow density and fabrication simplicity, which holds promise for filling the remaining white space in the Ashby map of toughness versus density. In contrast to modulus and strength that are often bounded by the rule of mixtures, the fracture toughness of lattice materials is not theoretically limited by this prediction. In principle, it should be possible to design lattice materials to achieve exceptional toughness far superior to that of their constituent materials. In this study, the fabricated Schwarz P shell lattices have exhibited fracture initiation toughness surpassing that of the parent material by ~90% while having a density ~62% lower. Despite this notable enhancement, we have not yet reached the white space in the toughness-versus-density Ashby map. Further efforts can be dedicated to achieving metamaterials with unprecedented toughness in the lightweight regime by architecting toughening mechanisms across various length scales. This will rely on the design of optimal architectures, the selection of suitable constituent materials, and the utilization of size effects in nanomaterials as well as structural hierarchy.

We experimentally characterized the fracture resistance of 3D shell-based lattice metamaterials with Schwarz P minimal surface topology and compared their fracture behaviors with conventional octet truss lattices. Our experiments demonstrated that Schwarz P shell lattices exhibited superior fracture initiation toughness and enhanced resistance to crack propagation, compared to the octet truss lattices in which the cracks tend to advance through the nodes due to severe stress concentration. The fabricated Schwarz P shell lattices exhibited fracture initiation toughness exceeding that of the constituent material while maintaining a lower density. FE simulations revealed that the superior fracture resistance in Schwarz P shell lattices can be attributed to the topology-induced toughening mechanism that amplify material damage dissipation, nonrecoverable elastic dissipation, and material plastic dissipation facilitated by the mechanically efficient topology, inherently enabling a larger process zone. Our study demonstrates the intrinsic toughening mechanism in shell-based lattice metamaterials and sheds light on the potential mechanomaterial route to achieving exceptional fracture toughness in the lightweight regime through tailored design of lattice metamaterials.

MATERIALS AND METHODS

Fabrication

CT fracture specimens were fabricated from commercial HTL resin (BMF Precision Technology Co. Ltd., China) using a microArch S140 PμSL system (BMF Precision Technology Co. Ltd., China). During fabrication, the printing layer thickness was 10 μm. The printing direction was along the direction of the sample thickness. The exposure intensity and exposure time for each layer were 30 mW cm^{-2} and 1.8 s, respectively. The printed samples were first immersed in 99% ethanol for 1 min in an ultrasonic bath to eliminate any uncured resin and then dried in a vacuum for 10 min. After cleaning and drying, the samples were post-cured for 5 min under 405-nm ultraviolet light. The overall dimensions of the CT specimens were designed on the basis of ASTM E1820 (*44*), with $W = 15$ mm and $B = 7.5$ mm. The lattice CT specimens were composed of octet truss or Schwarz P shell unit cells with $L = 1.5$ mm, resulting in $W = 10L$ and $B = 5L$. A precrack with length of $a_0 = 3L = 4.5$ mm and height of 0.1 mm was incorporated into the sliced images and directly printed. Solid rings with thickness of 0.45 mm were introduced around the loading pin holes to reinforce the local structure and prevent lattice damage. The relative density of the fabricated lattice metamaterial was calculated by dividing its density by the material density ($\rho_s = 1.27$ g cm^{-3}), which was determined from a fully dense solid HTL sample. The density of the lattice metamaterial was calculated by dividing the mass by its occupied volume, where the mass was determined by excluding the mass of the solid reinforcing rings (estimated by multiplying the designed volume of solid rings by ρ_s) from the total sample mass measured using a precision balance. A recent study suggested that a sufficiently large number of unit cells is required to characterize fracture toughness of lattice metamaterials (*32*). Considering the substantial increase in printing time with larger samples, our CT specimens were designed with $W = 10L$ and consisted of 750 unit cells, which are considered to be adequate for providing meaningful comparisons between different lattice structures. To confirm this, we also fabricated larger lattice CT specimens with $W = 20L$ and showed that the measured fracture toughness of these larger samples was comparable to that obtained from CT specimens with $W = 10L$ (fig. S11).

Mechanical testing

Fracture tests were performed using a universal testing machine with a 10-kN load cell (AG-X plus, Shimadzu Corp., Japan) at a constant displacement rate of 1.0 mm min^{-1}. During the test, videos were recorded and used to obtain the crack length (with one-half–unit cell resolution) (*34*). The obtained crack length and the force versus load-line displacement data were used to calculate the fracture toughness and *R*-curves.

Fracture toughness calculation

Fracture toughness and *R*-curves were calculated using the *J*-integral method following the procedure suggested by ASTM E1820 (*44*). The *J*-integral at each crack extension instant (i) was calculated by adding the elastic part $J_{el(i)}$ and the plastic part $J_{pl(i)}$. The elastic component is related to stress intensity factor $K_{(i)}$ as $J_{el(i)} = K_{(i)}^2 / E$, where E is the effective modulus of the lattice metamaterials. $K_{(i)}$ was obtained by the recorded force $P_{(i)}$ as

$$K_{(i)} = \frac{P_{(i)}}{B\sqrt{W}} f\left(\frac{a_{(i)}}{W}\right)$$

where $a_{(i)}$ is the crack length at the instant (i) and the calibration factor was calculated as

$$f\left(\frac{a_{(i)}}{W}\right) = \frac{\left(2+\frac{a_{(i)}}{W}\right)\left[0.886+4.64\left(\frac{a_{(i)}}{W}\right)-13.32\left(\frac{a_{(i)}}{W}\right)^2+14.72\left(\frac{a_{(i)}}{W}\right)^3-5.6\left(\frac{a_{(i)}}{W}\right)^4\right]}{\left(1-\frac{a_{(i)}}{W}\right)^{3/2}}$$

Effective modulus of the lattice metamaterial was obtained from the power law scaling relationship with the relative density as $E = \alpha E_s \bar{\rho}^m$, where α and m are constants depending on lattice topology and E_s is the Young's modulus of the constituent material. The coefficient α and the exponent m for octet truss and Schwarz P shell topology were taken from the previous study (*35*). The Young's modulus

E_s = 2.65 GPa was obtained from tensile tests on solid dogbone specimens in accordance with ASTM D638 (fig. S12). The plastic component $J_{\mathrm{pl}(i)}$ was calculated using an incremental approach

$$J_{\mathrm{pl}(i)} = \left[J_{\mathrm{pl}(i-1)} + \left(\frac{\eta_{\mathrm{pl}(i-1)}}{b_{(i-1)}}\right)\frac{\left(A_{\mathrm{pl}(i)} - A_{\mathrm{pl}(i-1)}\right)}{B}\right]\left[1 - \gamma_{(i-1)}\frac{a_{(i)} - a_{(i-1)}}{b_{(i-1)}}\right]$$

where A_{pl} is the plastic area under the force-displacement curve, $b_{(i-1)} = W - a_{(i-1)}$ is the remaining ligament, $\eta_{\mathrm{pl}(i-1)} = 2 + 0.522b_{(i-1)}/W$, and $\gamma_{(i-1)} = 1 + 0.76b_{(i-1)}/W$. The fracture toughness was calculated by $K_{J(i)} = \sqrt{EJ_{(i)}}$. Although the ASTM standard is established for continuous materials, this procedure was also used by many existing studies (*28*, *29*, *33*, *34*) to calculate the fracture toughness of truss-based lattices, in the absence of a universally accepted method for evaluating lattice material toughness. The apparent/effective toughness derived from the ASTM standard can provide meaningful comparisons between lattice materials and continuous materials, as well as across different lattice designs.

FE simulation

FE simulations were performed via Abaqus/Explicit (Dassault Systèmes SE). Two series of simulations were conducted. In the first scenario, octet truss lattices and Schwarz P shell lattices were modeled using three-noded quadratic Timoshenko beam elements (B32 in Abaqus) and three-noded triangular shell elements (S3 in Abaqus), respectively. The overall dimensions of the simulated models were consistent with those of the CT specimens used in experiments. To ensure high accuracy, each strut in octet truss lattices was discretized using seven B32 beam elements, and each unit cell in Schwarz P shell lattices was discretized with 1104 S3 shell elements. Consequently, the simulated models for octet truss lattices and Schwarz P shell lattices comprised ~19 million and ~86 million elements, respectively. The material was modeled as an elastoplastic material with a Young's modulus of 2.65 GPa and a Poisson's ratio of 0.4 in the linear elastic region and plastic behavior described by the Ramberg-Osgood relationship in the plastic region, which were taken from those of the polymer used in the experiments (see fig. S12 for details). To simulate fracture of the constituent material through element removal, a damage model was used, characterized by a plastic fracture strain of 0.026 and linear damage evolution determined by a fracture energy of 0.8 kJ m^{-2}. The plastic fracture strain of 0.026, combined with the elastic limit strain of 0.012, results in a total fracture strain of 0.038, consistent with the average value obtained from experiments (fig. S12). The nodes on the surfaces of the two pin holes were kinematically coupled with two respective reference points. Free rotation boundary conditions were applied by allowing rotations around the out-of-plane axis to be unconstrained. To investigate crack propagation, each model was loaded until fracture occurred in at least five unit cells (fig. S5). In the second scenario, to quantify contributions from different mechanisms, four-noded linear tetrahedron solid elements (C3D4 in Abaqus) were used for both octet truss and Schwarz P shell lattices. The in-plane dimensions were kept the same as those in experiments, while the thickness was set as $B = L$ to mitigate computational costs. The simulated models for octet truss and Schwarz P shell lattices with a relative density of ~30% were composed of ~6 million elements. Two material behaviors were considered. One is an ideally brittle material with a Young's modulus of 410 GPa and a strength of 550 MPa, taken from the values of silicon carbide, hence representative of elastic brittle ceramics (*47*). The fracture energy was set as 1 J m^{-2}, which is a typical value of brittle materials. The other material behavior is ductile, identical to that used in the first scenario. The models were loaded until crack propagated by one unit cell. The energy outputs were used to calculate fracture energies. In fracture mechanics, the energy release rate is defined as the energy available for an infinitesimal crack extension, given by $G = -\frac{1}{B}\left(\frac{dU_e}{da}\right)_{\Delta}$ for displacement-controlled structure, where U_e is the elastic strain energy and B is the thickness (*23*). The criterion for crack extension is $G = G_c = \Gamma$. Here, to estimate the critical energy release rate and components of fracture energy, we considered energy variations due to finite crack extension of half or one unit cell instead of infinitesimal crack extension. This is considered reasonable because cracks always propagate by half or one unit cell in lattice materials. Therefore, Γ, Γ_0, Γ_{NE}, and Γ_{P} can be numerically estimated as

$$\Gamma \approx -\frac{\Delta U_e}{B\Delta a}, \Gamma_0 \approx \frac{\Delta U_{\mathrm{DMD}}}{B\Delta a}, \Gamma_{\mathrm{NE}} \approx \frac{\Delta U_{\mathrm{VD}}}{B\Delta a}, \Gamma_{\mathrm{P}} \approx \frac{\Delta U_{\mathrm{PD}}}{B\Delta a}$$

where ΔU_e, ΔU_{DMD}, ΔU_{VD}, and ΔU_{PD} are the changes in strain energy, damage dissipation, viscous dissipation, and plastic dissipation, respectively (see figs. S7 and S8).

Supplementary Materials

This PDF file includes:

Figs. S1 to S12
Tables S1 and S2
Legends for movies S1 to S3

Other Supplementary Material for this manuscript includes the following:

Movies S1 to S3

REFERENCES AND NOTES

1. L. J. Gibson, M. F. Ashby, *Cellular Solids: Structure and Properties* (Cambridge Univ. Press, 1999).
2. A. G. Evans, J. W. Hutchinson, N. A. Fleck, M. F. Ashby, H. N. G. Wadley, The topological design of multifunctional cellular metals. *Prog. Mater. Sci.* **46**, 309–327 (2001).
3. N. A. Fleck, V. S. Deshpande, M. F. Ashby, Micro-architectured materials: Past, present and future. *Proc. R. Soc. A.* **466**, 2495–2516 (2010).
4. J. Bauer, L. R. Meza, T. A. Schaedler, R. Schwaiger, X. Zheng, L. Valdevit, Nanolattices: An emerging class of mechanical metamaterials. *Adv. Mater.* **29**, 1701850 (2017).
5. X. Zhang, Y. Wang, B. Ding, X. Li, Design, fabrication, and mechanics of 3D micro–/nanolattices. *Small* **16**, e1902842 (2020).
6. P. Cai, C. Wang, H. Gao, X. Chen, Mechanomaterials: A rational deployment of forces and geometries in programming functional materials. *Adv. Mater.* **33**, e2007977 (2021).
7. G. Zou, C. H. Sow, Z. Wang, X. Chen, H. Gao, Mechanomaterials and nanomechanics: Toward proactive design of material properties and functionalities. *ACS Nano* **18**, 11492–11502 (2024).
8. T. A. Schaedler, A. J. Jacobsen, A. Torrents, A. E. Sorensen, J. Lian, J. R. Greer, L. Valdevit, W. B. Carter, Ultralight metallic microlattices. *Science* **334**, 962–965 (2011).
9. X. Zheng, H. Lee, T. H. Weisgraber, M. Shusteff, J. DeOtte, E. B. Duoss, J. D. Kuntz, M. M. Biener, Q. Ge, J. A. Jackson, S. O. Kucheyev, N. X. Fang, C. M. Spadaccini, Ultralight, ultrastiff mechanical metamaterials. *Science* **344**, 1373–1377 (2014).
10. J. B. Berger, H. N. Wadley, R. M. McMeeking, Mechanical metamaterials at the theoretical limit of isotropic elastic stiffness. *Nature* **543**, 533–537 (2017).
11. J. Ye, L. Liu, J. Oakdale, J. Lefebvre, S. Bhowmick, T. Voisin, J. D. Roehling, W. L. Smith, M. R. Ceron, J. van Ham, L. B. Bayu Aji, M. M. Biener, Y. M. Wang, P. R. Onck, J. Biener, Ultra-low-density digitally architected carbon with a strutted tube-in-tube structure. *Nat. Mater.* **20**, 1498–1505 (2021).
12. Y. Wang, F. Xu, H. Gao, X. Li, Elastically isotropic truss-plate-hybrid hierarchical microlattices with enhanced modulus and strength. *Small* **19**, e2206024 (2023).
13. J. Bauer, A. Schroer, R. Schwaiger, O. Kraft, Approaching theoretical strength in glassy carbon nanolattices. *Nat. Mater.* **15**, 438–443 (2016).

14. X. Zhang, A. Vyatskikh, H. Gao, J. R. Greer, X. Li, Lightweight, flaw-tolerant, and ultrastrong nanoarchitected carbon. *Proc. Natl. Acad. Sci. U.S.A.* **116**, 6665–6672 (2019).
15. C. Crook, J. Bauer, A. Guell Izard, C. Santos de Oliveira, E. S. J. Martins de Souza, J. B. Berger, L. Valdevit, Plate-nanolattices at the theoretical limit of stiffness and strength. *Nat. Commun.* **11**, 1579 (2020).
16. L. R. Meza, S. Das, J. R. Greer, Strong, lightweight, and recoverable three-dimensional ceramic nanolattices. *Science* **345**, 1322–1326 (2014).
17. L. R. Meza, A. J. Zelhofer, N. Clarke, A. J. Mateos, D. M. Kochmann, J. R. Greer, Resilient 3D hierarchical architected metamaterials. *Proc. Natl. Acad. Sci. U.S.A.* **112**, 11502–11507 (2015).
18. X. Zhang, J. Yao, B. Liu, J. Yan, L. Lu, Y. Li, H. Gao, X. Li, Three-dimensional high-entropy alloy-polymer composite nanolattices that overcome the strength-recoverability trade-off. *Nano Lett.* **18**, 4247–4256 (2018).
19. Q. Li, J. Kulikowski, D. Doan, O. A. Tertuliano, C. J. Zeman, M. M. Wang, G. C. Schatz, X. W. Gu, Mechanical nanolattices printed using nanocluster-based photoresists. *Science* **378**, 768–773 (2022).
20. C. M. Portela, B. W. Edwards, D. Veysset, Y. Sun, K. A. Nelson, D. M. Kochmann, J. R. Greer, Supersonic impact resilience of nanoarchitected carbon. *Nat. Mater.* **20**, 1491–1497 (2021).
21. Y. Kai, S. Dhulipala, R. Sun, J. Lem, W. DeLima, T. Pezeril, C. M. Portela, Dynamic diagnosis of metamaterials through laser-induced vibrational signatures. *Nature* **623**, 514–521 (2023).
22. T. Butruille, J. C. Crone, C. M. Portela, Decoupling particle-impact dissipation mechanisms in 3D architected materials. *Proc. Natl. Acad. Sci. U.S.A.* **121**, e2313962121 (2024).
23. T. L. Anderson, *Fracture Mechanics: Fundamentals and Applications* (CRC Press, 2017).
24. J. S. Huang, L. J. Gibson, Fracture toughness of brittle honeycombs. *Acta Metall. Mater.* **39**, 1617–1626 (1991).
25. N. A. Fleck, X. Qiu, The damage tolerance of elastic–brittle, two-dimensional isotropic lattices. *J. Mech. Phys. Solids* **55**, 562–588 (2007).
26. N. E. R. Romijn, N. A. Fleck, The fracture toughness of planar lattices: Imperfection sensitivity. *J. Mech. Phys. Solids* **55**, 2538–2564 (2007).
27. H. C. Tankasala, V. S. Deshpande, N. A. Fleck, 2013 Koiter medal paper: Crack-tip fields and toughness of two-dimensional elastoplastic lattices. *J. Appl. Mech.* **82**, 091004 (2015).
28. M. R. O'Masta, L. Dong, L. St-Pierre, H. N. G. Wadley, V. S. Deshpande, The fracture toughness of octet-truss lattices. *J. Mech. Phys. Solids* **98**, 271–289 (2017).
29. H. Gu, S. Li, M. Pavier, M. M. Attallah, C. Paraskevoulakos, A. Shterenlikht, Fracture of three-dimensional lattices manufactured by selective laser melting. *Int. J. Solids Struct.* **180–181**, 147–159 (2019).
30. S. Daynes, J. Lifton, W. F. Lu, J. Wei, S. Feih, Fracture toughness characteristics of additively manufactured Ti-6Al-4V lattices. *Eur. J. Mech. A Solids* **86**, 104170 (2021).
31. T. Li, F. Jarrar, R. Abu Al-Rub, W. Cantwell, Additive manufactured semi-plate lattice materials with high stiffness, strength and toughness. *Int. J. Solids Struct.* **230–231**, 111153 (2021).
32. A. J. D. Shaikeea, H. Cui, M. O'Masta, X. R. Zheng, V. S. Deshpande, The toughness of mechanical metamaterials. *Nat. Mater.* **21**, 297–304 (2022).
33. M. Maurizi, B. W. Edwards, C. Gao, J. R. Greer, F. Berto, Fracture resistance of 3D nano-architected lattice materials. *Extreme Mech. Lett.* **56**, 101883 (2022).
34. B. C. White, A. Garland, B. L. Boyce, Toughening by interpenetrating lattices. *Matter* **6**, 570–582 (2023).
35. Y. Wang, X. Zhang, Z. Li, H. Gao, X. Li, Achieving the theoretical limit of strength in shell-based carbon nanolattices. *Proc. Natl. Acad. Sci. U.S.A.* **119**, e2119536119 (2022).
36. A. Guell Izard, J. Bauer, C. Crook, V. Turlo, L. Valdevit, Ultrahigh energy absorption multifunctional spinodal nanoarchitectures. *Small* **15**, e1903834 (2019).
37. C. M. Portela, A. Vidyasagar, S. Krodel, T. Weissenbach, D. W. Yee, J. R. Greer, D. M. Kochmann, Extreme mechanical resilience of self-assembled nanolabyrinthine materials. *Proc. Natl. Acad. Sci. U.S.A.* **117**, 5686–5693 (2020).
38. S. Kumar, S. Tan, L. Zheng, D. M. Kochmann, Inverse-designed spinodoid metamaterials. *npj Comput. Mater.* **6**, 73 (2020).
39. F. V. Senhora, E. D. Sanders, G. H. Paulino, Optimally-tailored spinodal architected materials for multiscale design and manufacturing. *Adv. Mater.* **34**, e2109304 (2022).
40. S. Hyde, Z. Blum, T. Landh, S. Lidin, B. Ninham, S. Andersson, K. Larsson, *The Language of Shape: The Role of Curvature in Condensed Matter: Physics, Chemistry and Biology* (Elsevier, 1996).
41. S. C. Han, J. W. Lee, K. Kang, A new type of low density material: Shellular. *Adv. Mater.* **27**, 5506–5511 (2015).
42. V. S. Deshpande, N. A. Fleck, M. F. Ashby, Effective properties of the octet-truss lattice material. *J. Mech. Phys. Solids* **49**, 1747–1769 (2001).
43. K. A. Brakke, The surface evolver. *Exp. Math.* **1**, 141–165 (1992).
44. E08 Committee, *E1820 Standard Test Method for Measurement of Fracture Toughness* (ASTM International, 2017).
45. J. Blaber, B. Adair, A. Antoniou, Ncorr: Open-source 2D digital image correlation Matlab software. *Exp. Mech.* **55**, 1105–1122 (2015).
46. W. Zhang, H. Ye, X. Feng, W. Zhou, K. Cao, M. Li, S. Fan, Y. Lu, Tailoring mechanical properties of PμSL 3D-printed structures via size effect. *Int. J. Extrem. Manuf.* **4**, 045201 (2022).
47. M.-T. Hsieh, V. S. Deshpande, L. Valdevit, A versatile numerical approach for calculating the fracture toughness and R-curves of cellular materials. *J. Mech. Phys. Solids* **138**, 103925 (2020).

Acknowledgments: We would like to acknowledge the Facility for Analysis, Characterisation, Testing and Simulation, Nanyang Technological University, Singapore, for use of electron microscopy facilities. **Funding:** H.G. acknowledges a research start-up grant from the Nanyang Technological University (00247900001) and the Agency for Science, Technology and Research (A*STAR). Yifan Wang acknowledges the NAP award (020482) from Nanyang Technological University. X.L. acknowledges financial support from the National Natural Science Foundation of China (grant number 12325203). X.Z. acknowledges financial support from the Fundamental Research Funds for the Central Universities, Peking University. **Author contributions:** Conceptualization: Yujia Wang and H.G. Methodology: Yujia Wang and H.G. Investigation: Yujia Wang, K.W., and X.Z. Formal analysis: Yujia Wang and H.G. Visualization: Yujia Wang. Supervision: X.L., Yifan Wang, and H.G. Funding acquisition: X.Z., X.L., Yifan Wang, and H.G. Writing—original draft: Yujia Wang. Writing—review and editing: Yujia Wang, X.L., Yifan Wang, and H.G. **Competing interests:** The authors declare that they have no competing interests. **Data and materials availability:** All data needed to evaluate the conclusions in the paper are present in the paper and/or the Supplementary Materials.

Submitted 9 May 2024
Accepted 25 July 2024
Published 30 August 2024
10.1126/sciadv.adq2664